Improved Synthesis and Transient Absorption Spectroscopy of $CuBiW_2O_8$ with Demonstration of Visible-Light-Driven Photocatalysis and Mechanistic Insights

Ceren Yilmaz Akkaya[a], James Dombrowski,[a] Erika Colin-Ulloa,[b] Lyubov V. Titova,[b] Timothy J. Lawton,[c]
Todd Alexander,[c] Eric Brack,[c] Christopher Drew,[c] Pratap M. Rao[a] *

[a]Department of Mechanical Engineering, Worcester Polytechnic Institute, Worcester, Massachusetts, 01609, USA
[b]Department of Physics, Worcester Polytechnic Institute, Worcester, Massachusetts, 01609, USA
[c]Soldier Protection Directorate, US Army Combat Capabilities Development Command Soldier Center, Natick, Massachusetts, 01760, USA
**Corresponding Author: E-mail address: pmrao@wpi.edu (Pratap M. Rao)*

Supporting Information

Table of Contents

Table of Figures

1. Synthesis Procedure and Optimization of the Synthesis to Obtain **Cu_2WO_4 as Precursor**

1.1 Synthesis of $CuWO_4$

The $CuWO_4$ microcrystals were synthesized by following a reported procedure.[1] CuO (10 mmol) and WO_3 (10 mmol) were ground to a uniform powder by mortar and pestle before the mixture was transferred to an open-top high-alumina cup crucible and placed in a box oven under ambient atmosphere. The sample was heated to 800 °C (3 h ramp time) before being held isothermally for 12 hours and left to cool ambiently to ~20 °C. The ochre-colored homogeneous powder was collected and ground by mortar and pestle to a fine powder. The observed Raman-active modes and XRD peaks for the obtained product are in line with the published data indicating highly crystalline, pure, triclinic $CuWO_4$ (Fig. S1)[2].

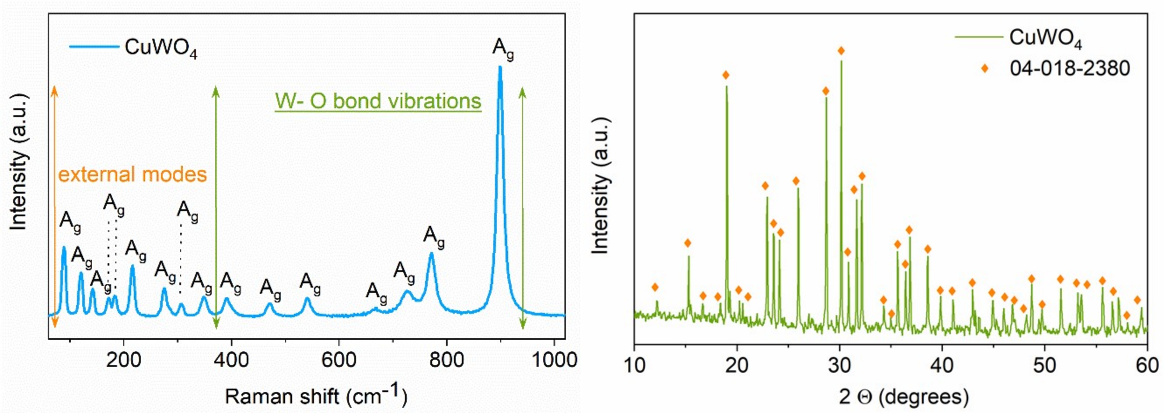

Fig. S1 Raman spectrum (left) and powder XRD diagram (right) of $CuWO_4$ (standard pattern (ICDD PDF 04-018-2380) is also included for comparison)

1.2 Synthesis of Cu_2WO_4

Cu_2WO_4 was synthesized by comproportionation of elemental copper (metal powder, 5 µm) and $CuWO_4$ under Argon. There are only a few studies on Cu_2WO_4 with the majority focusing on rapid high temperature flux syntheses facilitated by an electric arc or laser heating.[3–5] To optimize the solid-state reaction route, experiments were performed with two different copper sources. The initial experiments were performed with ~ 2-3 mm squares of Cu^0 foil (0.127 mm thick). However, the product was contaminated with unreacted residual foil following thermal treatments. Hence, the following studies were conducted with copper powder of 5 µm size. $CuWO_4$ (3.2 mmol) and Cu^0 powder (3.2 mmol) were ground for 30 min. to a uniform powder by mortar and pestle before the thermal treatment at 650 °C (30 min ramp, 8 h isothermal, ambient cooling) under an argon atmosphere (300 cc/min) in a one-zone tube furnace. A copper-foil cover was placed on top of the high alumina combustion boat to act as a sacrificial reductant for any trace O_2 contamination in the argon. Reacting the ground mixture of copper metal powder (5 µm) and $CuWO_4$ at around the melting temperature of the product yielded phase pure maroon colored, rod-like Cu_2WO_4 crystals with preferred orientation as indicated by the preferential exposure of the (101) plane. (Fig. S2).

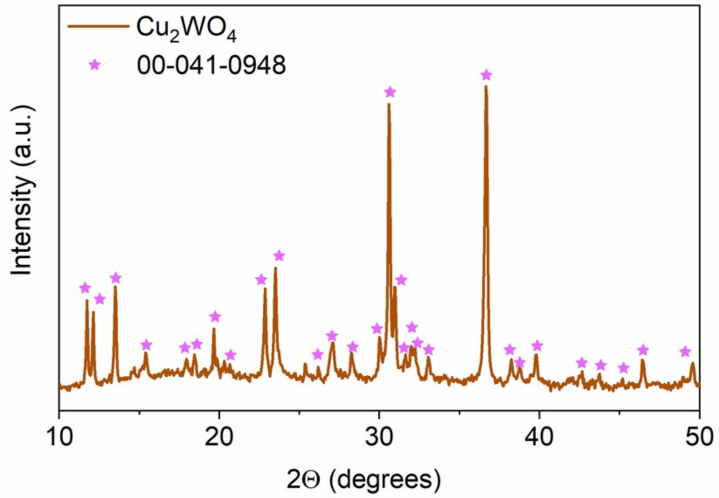

Fig. S2 XRD diagram of Cu_2WO_4 prepared by comproportionation of copper metal powder (5 µm) and $CuWO_4$ (standard pattern (ICDD PDF 00-041-0948) is also included for comparison)

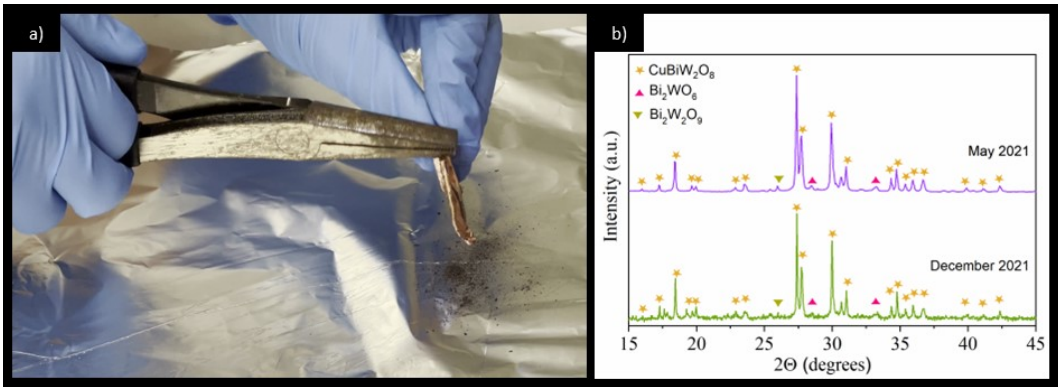

Fig. S3 (a) CBTO powder collected by opening the copper box, inverting it, and tapping, (b) XRD patterns of the collected CBTO powder prepared by Cu_2WO_4 based route at 800 °C for 4 h in Cu rich atmosphere by different scientists six months apart

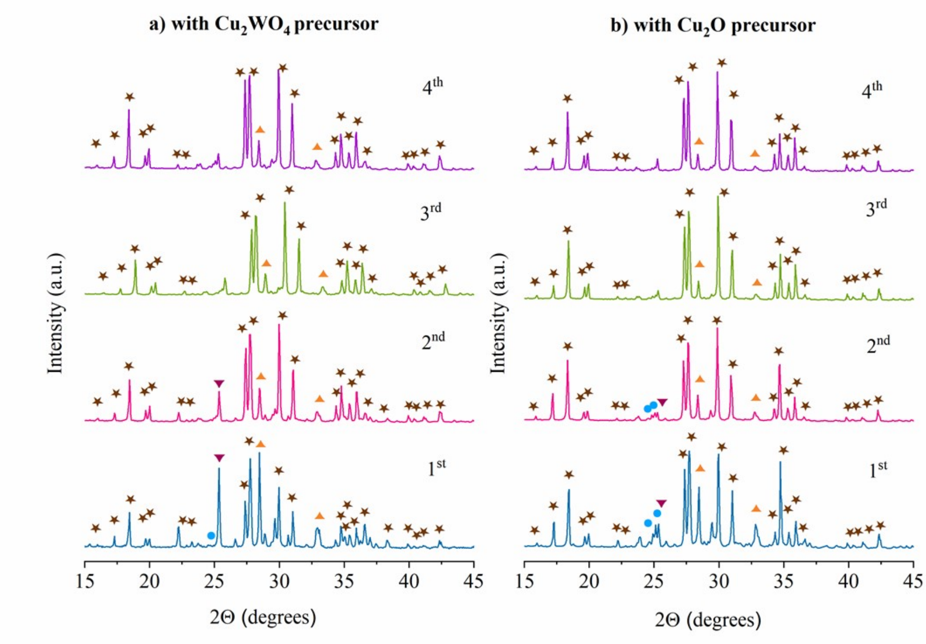

Fig. S4 Comparison of the XRD diagrams of CBTO prepared by annealing 4 times at 600 °C for 9 hours with intermittent ball milling after each annealing with a) Cu_2WO_4 or b) Cu_2O as ternary and binary precursors in Cu rich atmosphere (★ CBTO, ▲ Bi_2WO_6, ▼ $Bi_2W_2O_9$, ● WO_3)

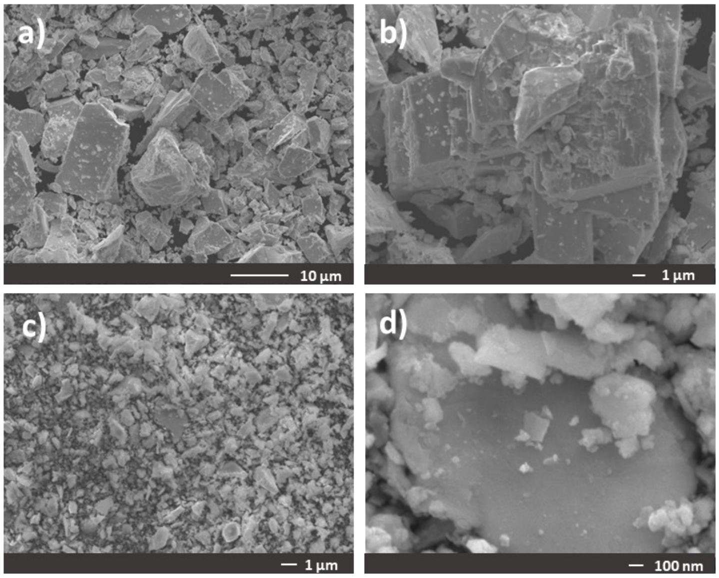

Fig. S5 SEM images of CBTO prepared by Cu_2WO_4 based route at 800 °C for 4 h in Cu rich atmosphere (a,b) as-synthesized and (c,d) after ball milling

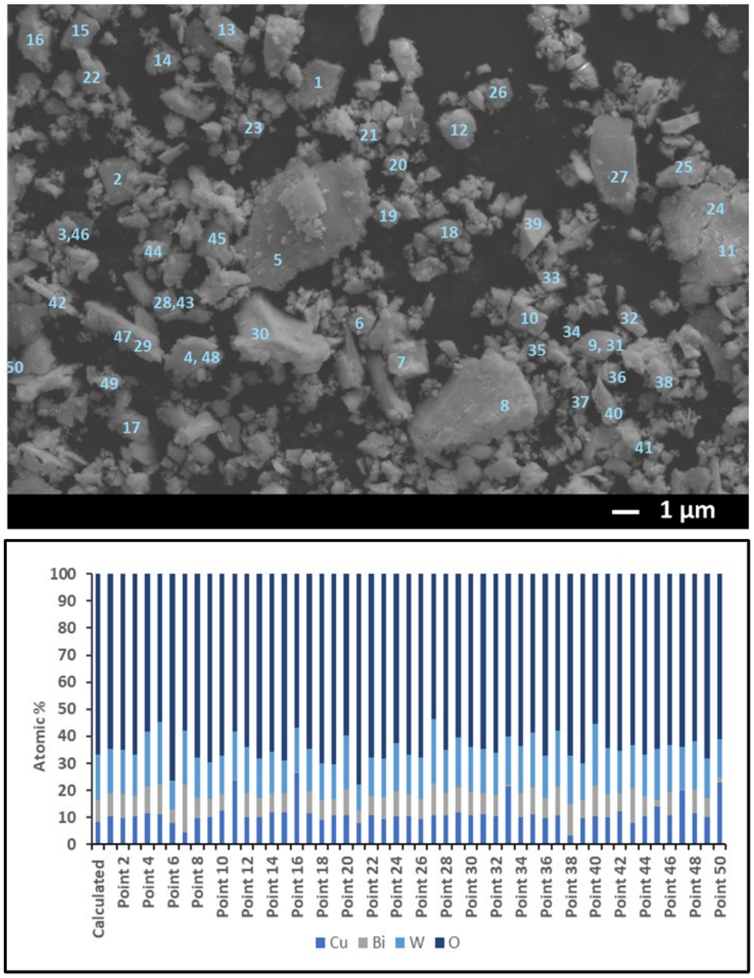

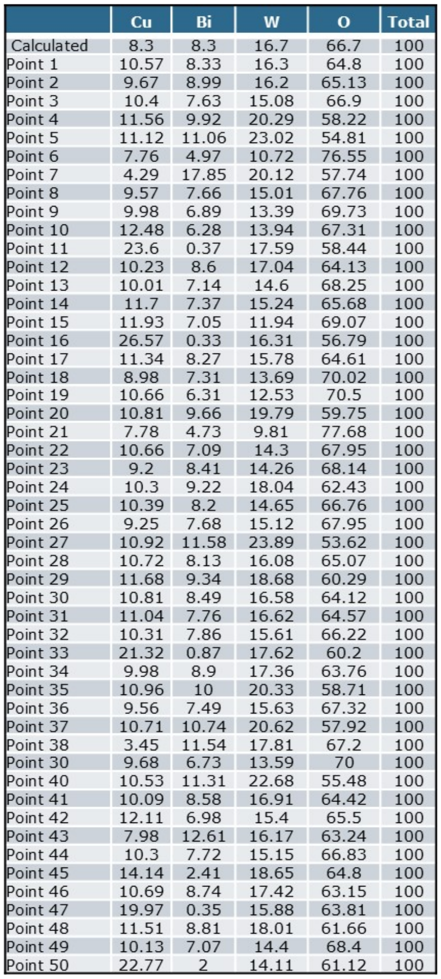

	Cu	Bi	W	O	Total
Calculated	8.3	8.3	16.7	66.7	100
Point 1	10.57	8.33	16.3	64.8	100
Point 2	9.67	8.99	16.2	65.13	100
Point 3	10.4	7.63	15.08	66.9	100
Point 4	11.56	9.92	20.29	58.22	100
Point 5	11.12	11.06	23.02	54.81	100
Point 6	7.76	4.97	10.72	76.55	100
Point 7	4.29	17.85	20.12	57.74	100
Point 8	9.57	7.66	15.01	67.76	100
Point 9	9.98	6.89	13.39	69.73	100
Point 10	12.48	6.28	13.94	67.31	100
Point 11	23.6	0.37	17.59	58.44	100
Point 12	10.23	8.6	17.04	64.13	100
Point 13	10.01	7.14	14.6	68.25	100
Point 14	11.7	7.37	15.24	65.68	100
Point 15	11.93	7.05	11.94	69.07	100
Point 16	26.57	0.33	16.31	56.79	100
Point 17	11.34	8.27	15.78	64.61	100
Point 18	8.98	7.31	13.69	70.02	100
Point 19	10.66	6.31	12.53	70.5	100
Point 20	10.81	9.66	19.79	59.75	100
Point 21	7.78	4.73	9.81	77.68	100
Point 22	10.66	7.09	14.3	67.95	100
Point 23	9.2	8.41	14.26	68.14	100
Point 24	10.3	9.22	18.04	62.43	100
Point 25	10.39	8.2	14.65	66.76	100
Point 26	9.25	7.68	15.12	67.95	100
Point 27	10.92	11.58	23.89	53.62	100
Point 28	10.72	8.13	16.08	65.07	100
Point 29	11.68	9.34	18.68	60.29	100
Point 30	10.81	8.49	16.58	64.12	100
Point 31	11.04	7.76	16.62	64.57	100
Point 32	10.31	7.86	15.61	66.22	100
Point 33	21.32	0.87	17.62	60.2	100
Point 34	9.98	8.9	17.36	63.76	100
Point 35	10.96	10	20.33	58.71	100
Point 36	9.56	7.49	15.63	67.32	100
Point 37	10.71	10.74	20.62	57.92	100
Point 38	3.45	11.54	17.81	67.2	100
Point 30	9.68	6.73	13.59	70	100
Point 40	10.53	11.31	22.68	55.48	100
Point 41	10.09	8.58	16.91	64.42	100
Point 42	12.11	6.98	15.4	65.5	100
Point 43	7.98	12.61	16.17	63.24	100
Point 44	10.3	7.72	15.15	66.83	100
Point 45	14.14	2.41	18.65	64.8	100
Point 46	10.69	8.74	17.42	63.15	100
Point 47	19.97	0.35	15.88	63.81	100
Point 48	11.51	8.81	18.01	61.66	100
Point 49	10.13	7.07	14.4	68.4	100
Point 50	22.77	2	14.11	61.12	100

Fig. S6 Atomic % data from various points on ball-milled CBTO obtained by SEM - energy dispersive X-ray spectroscopy (EDS)

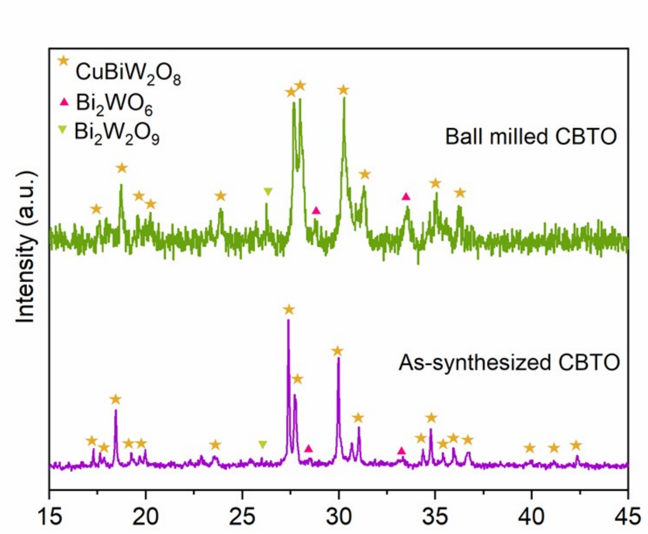

Fig. S7 XRD diagrams of as-synthesized and ball-milled CBTO powders

2. Optical and Photocatalytic Properties of CBTO

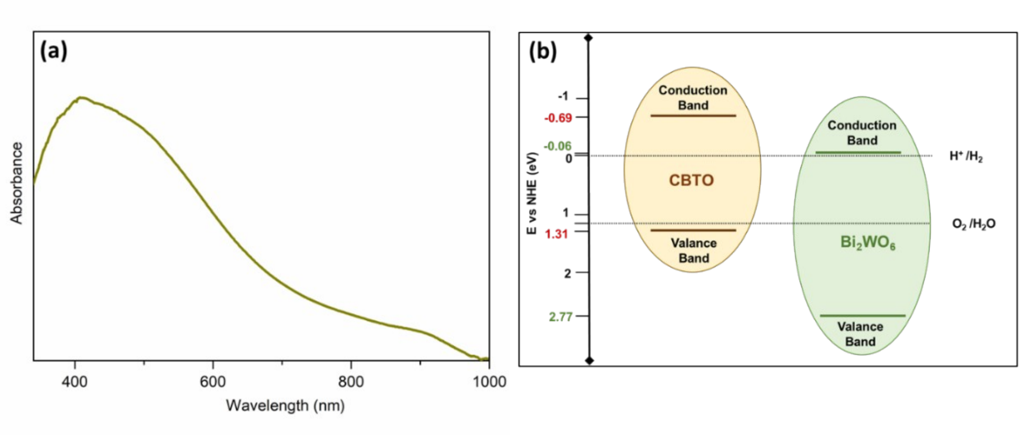

Fig. S8 (a) UV-Vis spectrum of CBTO powder dispersed in water. (b) Valence and conduction band edges of CBTO[6] and Bi_2WO_6[7]

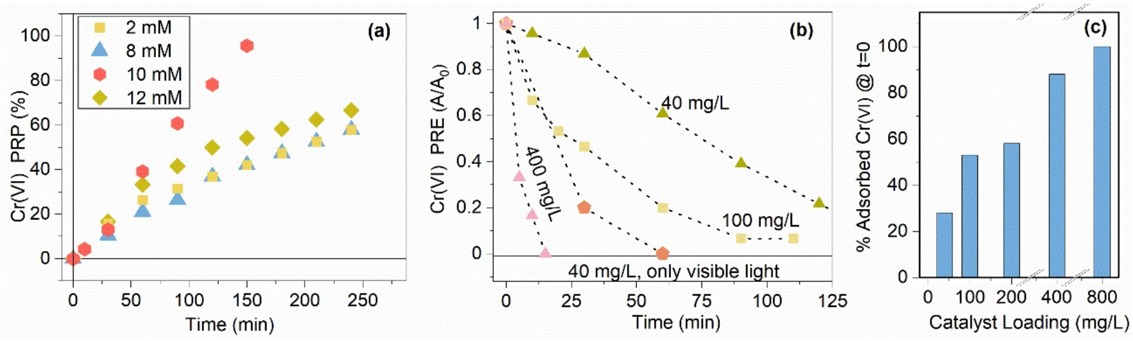

Fig. S9 Cr(VI) photoreduction with CBTO under excitation with 100 mW/cm^2 light , 40 ml of 5 mg/L Cr(VI) solution, 10 mM CA, pH=2 unless stated otherwise (a) influence of citric acid concentration, (b) influence of the catalyst loading and spectral irradiance, (c) percentage adsorption of Cr(VI) by CBTO in the dark at RT with varying catalyst loading .

The highest photoreduction efficiency was obtained with 400 mg/L catalyst loading. The photoreduction reaction was ~ 1.8-fold faster under only visible light, most probably due to the higher energy intensity with short band pass filter (FES0750) in the region where CBTO absorption is stronger (Fig. S8). Dark adsorption of Cr(VI) increases with catalyst loading reaching closer to ~100% in the presence of 800 mg/L catalyst.

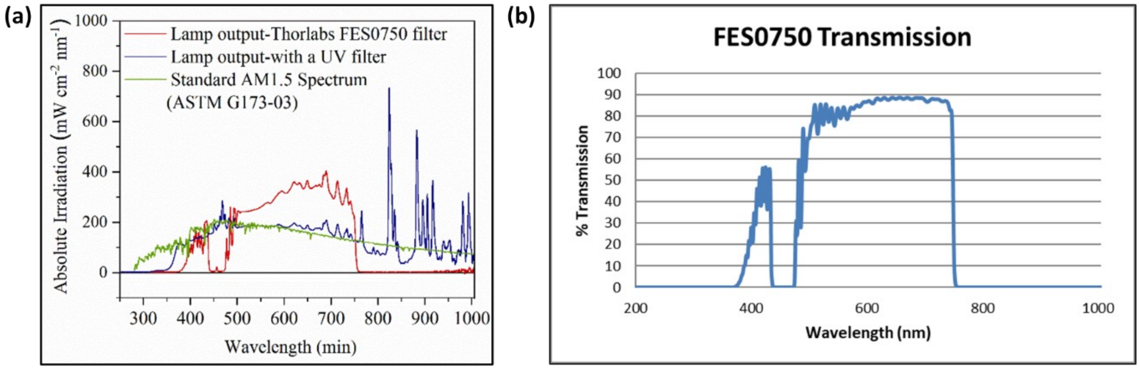

Fig. S10 (a) Spectrum of the 300 W Xe light source with a UV filter power adjusted to 100 mW/cm^2 and with a Thorlabs FES0750 filter powder adjusted to 90 mW/cm^2 as compared to ASTM G173-03 Reference Spectra Derived from SMARTS v. 2.9.2. (b) Transmission spectrum of a generic Thorlabs Ø1" (Ø25.4 mm) Shortpass Filter, Cut-On Wavelength: 750 nm (taken from the product website)

$$CuBiW_2O_8 + h\nu \rightarrow CuBiW_2O_8(e^- + h^+) \tag{S1}$$
$$Cr_2O_7^{2-} + 14H^+ + 6e^- \rightarrow 2Cr^{3+} + 7H_2O \tag{S2}$$
$$HCrO_4^- + 7H^+ + 3e^- \rightarrow Cr^{3+} + 4H_2O \tag{S3}$$
$$HCrO_4^- + 4H^+ + 3e^- \rightarrow Cr(OH)_3 + H_2O \tag{S4}$$
$$2HCrO_4^- + 8H^+ + 3e^- \rightarrow Cr_2O_3 + 5H_2O \tag{S5}$$
$$Cr_2O_7^{2-} + 8H^+ + 6e^- \rightarrow Cr_2O_3 + 4H_2O \tag{S6}$$
$$2H_2O + h^+ \rightarrow O_2 + 4H^+ \tag{S7}$$
$$O_2 + e^- \rightarrow O_2^{\bullet -} \tag{S8}$$
$$Cr(VI) + O_2^{\bullet -} \rightarrow Cr(III) + O_2 \tag{S9}$$
$$O_2^{\bullet -} + 2e^- + 2H^+ \rightarrow H_2O_2 \tag{S10}$$
$$H_2O_2 \rightarrow 2\ {}^{\bullet}OH \tag{S11}$$
$$O_2^{\bullet -} + 2e^- + 2H^+ \rightleftharpoons 2\ {}^{\bullet}OH \tag{S12}$$

Fig. S11 Possible reactions that might be involved in the Cr(VI) photoreduction with CBTO

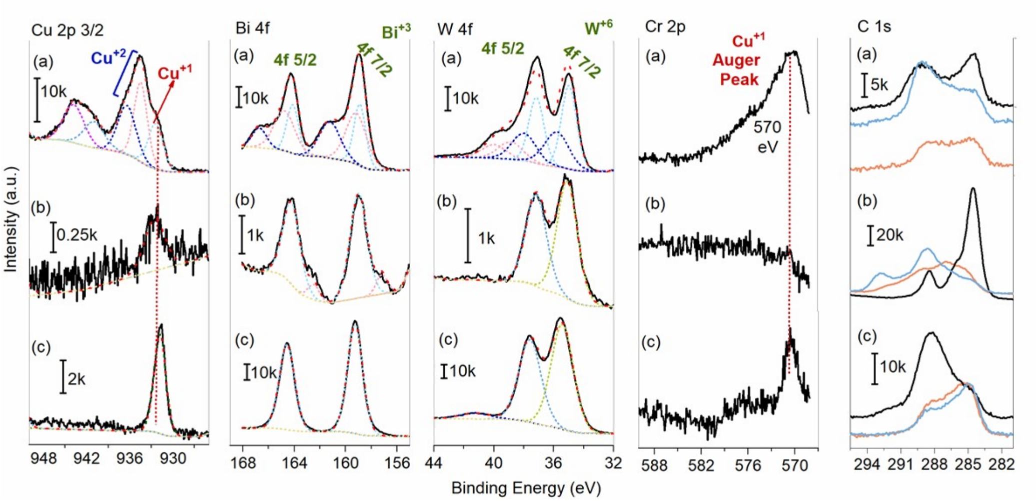

Fig. S12 X-Ray Photoelectron (XPS) spectra of CBTO (800 C,4h, Cu-rich environment, ball milled for 12h) (a) as-synthesized, (b) unwashed powder after the photocatalytic test, (c) powder washed with water and ethanol after the photocatalytic test. Dotted traces correspond to the fitted peaks for Cu 2p, Bi 4f, W 4f, and C 1s regions. (Spectra taken from 3 different points with 10 scans at each point is shown for the C 1s region; following colors are used to denote point 1,2, and 3, respectively: pink, black, and blue.)

The surface composition of CBTO and the chemical bonding states of the metals before and after the photocatalytic reaction in acidic medium as well as the presence of adsorbed Cr species on CBTO surface were examined by studying the Cu 2p, Bi 4f, W 4f and Cr 2p core level XPS spectra.

XPS spectrum in the Cu 2p region of the ball milled CBTO display three peaks at 932.4, 934.6, and 936.6 eV with strong shake-up peaks in the 940-945 eV region. The peaks around 932-934 eV are commonly observed for Cu^{2+} and those around 931-932 eV are attributed to Cu^{1+} in literature.[8,9] In addition, the high intensity satellite peak located around 9 eV higher binding energy than Cu $2p_{3/2}$ peak is typically observed in Cu^{2+} oxides.[10–12] Since Cu^{1+} and Cu peaks in the 2p region are very close to each other, generally X-Ray induced Cu LMM Auger lines around 570 eV are taken into consideration in distinguishing between these two states. The Cu $L_3M_{45}M_{45}$ line at 570.2 eV in Fig. S12a is a clear indication of Cu^{1+} species.[9,13,14] Hence, we ascribe the fitted peak at 932.4 to Cu^{1+} in CBTO and the peaks at 934.6, and 936.6 eV to Cu^{2+} oxide related impurities on CBTO surface, in line with our previous report.[6] It can be seen in Fig. S12a that three peaks appear in the Bi $4f_{7/2}$ (158.8, 159.2, 161.3 eV) and Bi $4f_{5/2}$ (164.1, 164.8, 166.7 eV) regions for CBTO before the reaction. It is known from the XRD patterns of CBTO (Fig. 2) that Bi_2WO_6 and $Bi_2W_2O_9$ impurities are present. Hence, these three sets of peaks can be ascribed to Bi^{3+} in different local chemical environments, likely generated by CBTO, Bi_2WO_6 and $Bi_2W_2O_9$.[15–17] Similarly, three sets of peaks appearing in the W $4f_{7/2}$ (34.9, 35.8, 37.1 eV) and W $4f_{5/2}$ (37.2, 37.7, 39.9 eV) regions can be attributed to W^{6+} likely generated by CBTO, Bi_2WO_6 and $Bi_2W_2O_9$.[18–21]

After the photocatalytic reaction, XPS features in Cu 2p, Bi 4f, and W 4f and regions due to the surface impurities disappear (Fig. S12b-c) indicating low stability of these materials under irradiation and/or in the acidic aqueous medium in line with previous reports. Early studies on photocatalytic stability of Bi_2WO_6 in acidic solutions ($pH < 5$) showed that Bi_2WO_6 is transformed into H_2WO_4 and Bi_2O_3 under visible light irradiation.[22] $Bi_2W_2O_9$ which is a layered material where perovskite like $[W_2O_7]^{2-}$slabs are separated by $[Bi_2O_2]^{2+}$ groups, is found to be susceptible to selective leaching in acidic environment giving rise to formation of layered tungstic compounds.[23–25] CuO is also reported to be unstable in acidic solutions.[26,27] At low pH, CuO is dissolved with significant Cu^{2+} leaching. Natural organic matter such as humic acid and citric acid also shown to improve dissolution of CuO particles.[28]

Moreover, no peak associated to Cr species appears to be present after the photocatalytic reaction (Fig. S12b-c). Cr 2p doublets due to Cr(VI) and Cr(III) features usually appear at binding energies of 579-589 eV and 577-586 eV, respectively.[29,30] In Fig S12b, no peaks appear in this region. The peak at around 570 eV present in Fig. S12c is due to the Cu $L_3M_{45}M_{45}$ Auger line as discussed above.

The change in the C 1s region spectra is also given in Fig.S12. 10-scan averages at 3 different physical locations were collected. For the unreacted CBTO, characteristic peaks of adventitious carbon contamination are seen at 284.8 eV (C-C) and 288.4 eV (C=O or C-O-C).[31] After the photocatalytic reaction, additional features appear at 286-287 eV and 290 eV (Fig. S12-13) which can be attributed to C-OH and carboxylic groups and in line with reported citric acid XPS data.[32] At point location 3, an additional strong peak at 292.9 eV appears which can be associated with alkali carboxylates[33] or K $2p_{3/2}$ peak in potassium carbonate/carboxylates.[34,35] This study does not exclude the possibility of reduced forms of citric acid being present on the surface of the catalyst.[32] A more detailed, time-dependent analysis is needed to monitor the relative intensity changes in the peaks associated with C-C,C=C,C-O-C, C-OH, C=O, and O-C-OH groups complemented with optical spectroscopy measurements.

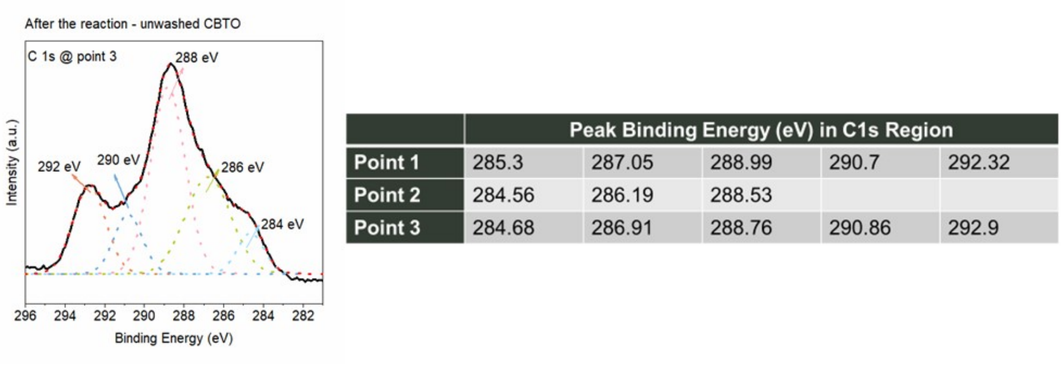

	Peak Binding Energy (eV) in C1s Region				
Point 1	285.3	287.05	288.99	290.7	292.32
Point 2	284.56	286.19	288.53		
Point 3	284.68	286.91	288.76	290.86	292.9

Figure S.13 C 1s region of unwashed CBTO after the reaction a) spectrum collected from point 3 and the fitted peaks (on the left), b) table displaying the binding energies of the fitted peaks in all 3 points

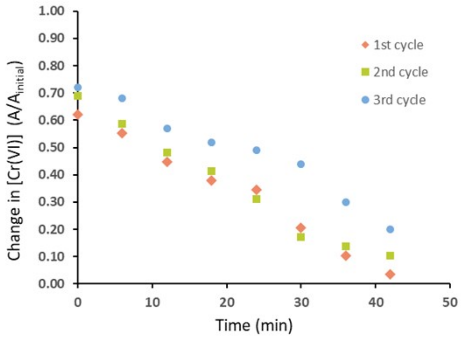

Figure S.14 Cr(VI) photoreduction with CBTO under excitation with 100 mW/cm^2 light , 40 ml of 5 mg/L Cr(VI) solution, 10 mM CA, pH=2, 200 mg/L CBTO.

3. Estimation of number of Cr(VI) ions to CBTO surface atom ratio

We have estimated the ratio of number of Cr(VI) ions to the number of CBTO surface atoms, for each photocatalytic test. The amount of Cr(VI) added in each photocatalytic test (5 mg/L in 40 mL volume) is a total of 2.3 × 10^{18} ions. As described in the manuscript, the CBTO particle size ranges from ~ 15 µm to 100 nm. Furthermore, the particles have smooth surfaces and are not porous. To find an upper limit for the number of CBTO surface atoms, we can assume that all the CBTO particles have the smallest diameter of 100 nm. The total number of surface atoms of CBTO (for 200 mg/L of CBTO in 40 mL volume) is then calculated to be 2.0 × 10^{17} atoms based on the primitive crystallographic unit cell volume of 157.4 Å^3. Therefore, the number of Cr(VI) ions that are photoreduced in each test is at least 10 times larger than the total number of CBTO surface atoms. Therefore, each active site on the CBTO photocatalyst surface is used many times during each photocatalytic Cr(VI) photoreduction test, suggesting that the CBTO photocatalyst is reusable. If a more realistic value of 1 µm is used for average CBTO particle diameter, the total number of surface atoms of CBTO is 2.0 × 10^{16} atoms, and the number of Cr(VI) ions is 100 times larger than the total number of surface atoms of CBTO for each photoreduction test.

Table S1 Photocatalytic Cr(VI) reduction activity of CBTO as compared to the photocatalysts reported in recent literature

Catalyst	**Catalyst Loading** (mg/L)	**Initial [Cr(VI)]** (mg/L)	**PRP**	**Time**	**Light Source**	**pH**	**Additives**	**Ref**
$CuBiW_2O_8$	200 400	5	~100 %	20 min 15 min	100 mW/cm^2 (300 W Xe lamp with UV filter)	2	10 mM Citric acid	This work
Bi_2O_3 / $CuBi_2O_4$ /Ag NP	400	10	96.9 %	30 min	Visible Light (250 W)	2	8 mM Citric acid	[36]
$CuFeO_2$	400	5	97	60 min	500 W Xe	3	80 mM Formic acid	[37]
Bi_2WO_6 porous nanosheets	1200	10	99.5 %	100 min	300 W Xe Visible light	-	480 mM Oxalic acid	[38]
Cu_2O / $BiVO_4$	500	0.08 mM	100 %	120 min	300 W Xe Visible light	-	-	[39]
$BiFe_4O_9$	750	25	100 %	180 min	200 W Tungsten	2	-	[40]
Au NP/ g-C_3N_4 nanosheet /$W_{18}O_{49}$	1000	20	87%	30 min	300 W Xe AM 1.5 visible light	-	6.9 mM Oxalic acid	[41]

4. References

1 Z. Wu, Z. Zhao, G. Cheung, R. M. Doughty, A. R. Ballestas-Barrientos, B. Hirmez, R. Han, T. Maschmeyer and F. E. Osterloh, *J Electrochem Soc*, 2019, **166**, H3014–H3019.

2 P. Yadav and E. Sinha, *Macromol Symp*, 2019, **388**, 1900019.

3 H. Mumm and H. MiiLLER-BUSCHBAUM Kiel, *Journal of the Less-Common Metals*, 1988, **142**, 85–90.

4 B. O. Marinder, P. L. Wang, P. E. Werner, M. Westdahl, A. F. Andersen and D. Louer, *Acta Chem. Scand.*, 1987, **A 41**, 152–157.

5 M. Tayar Galante, A. Živković, J. C. Alvim, C. C. Calchi Kleiner, M. Sangali, S. F. R. Taylor, A. J. Greer, C. Hardacre, K. Rajeshwar, R. Caram, R. Bertazzoli, R. T. Macaluso, N. H. de Leeuw and C. Longo, *ACS Appl Mater Interfaces*, 2021, **13**, 32865–32875.

6 L. Zhou, E. Bainglass, M. Masroor, B. Giri, G. Li, A. Carl, R. L. Grimm, M. N. Huda, L. v. Titova and P. M. Rao, *J Mater Chem A Mater*, 2021, **9**, 1643–1654.

7 B. Huang and J. N. Hart, *Physical Chemistry Chemical Physics*, 2020, **22**, 1727–1737.

8 J. Haber, T. Machej, L. Ungier and J. Zidekowski, *J Solid State Chem*, 1978, **25**, 207–218.

9 T. H. Fleisch and G. J. Mains, *Application of Surface Science*, 1982, **10**, 51–62.

10 S. Poulston, P. M. Parlett, P. Stone and M. Bowker, *Surface and Interface Analysis*, 1996, **24**, 811–820.

11 G. Morettit, G. Fierro, M. lo Jacono and P. Porta, *Surface and Interface Analysis*, 1989, **14**, 325–336.

12 J. Ghijsen, L. H. Tjeng, J. van Elp, H. Eskes, J. Westerink, G. A. Sawatzky and M. T. Czyzyk, *Phys Rev B*, 1988, **38**, 11322–11330.

13 Y. S. Lee, K. Y. Lim, D. Y. Chung and C. N. Whang, *Journal of Surface Analysis*, 1999, **5**, 204–207.

14 X. Zhang, M. Xia, F. Wang and W. Lei, *Ionics (Kiel)*, 2020, **26**, 6359–6369.

15 F. Wang, X. Zhou, J. Li, Q. He, L. Zheng, Q. Liu, Y. Chen, G. Zhang, X. Liu and H. Li, *Molecules*, 2021, **26**, 7334.

16 S. Kang, R. C. Pawar, Y. Pyo, V. Khare and C. S. Lee, *J Exp Nanosci*, 2016, **11**, 259–275.

17 D. Lahiri, S. Chattopadhyay, J. Kaduk, al -, H. Zhang, W. Zhao, H. Shi -, Y.-P. Wang, S.-S. Li and W.-X. Ji, *Jpn J Appl Phys*, 1992, **31**, L953–L955.

18 S. Rahimnejad, J. H. He, F. Pan, X. Lee, W. Chen, K. Wu and G. Q. Xu, *Mater Res Express*, 2014, **1**, 045044.

19 M. E. Pam, Y. Shi, J. Hu, X. Zhao, J. Dan, X. Gong, S. Huang, D. Geng, S. Pennycook, L. K. Ang and H. Y. Yang, *Nanoscale Adv*, 2019, **1**, 953–960.

20 B. V. R. Chowdari, K. L. Tan and W. T. Chia, *Solid State Ion*, 1992, 1172–1178.

21 G. E. McGUIRE, G. K. Schweitzer and and A. Thomas Carlson, *Inorg Chem*, 1973, **12**, 2450.

22 H. Fu, C. Pan, W. Yao and Y. Zhu, *Journal of Physical Chemistry B*, 2005, **109**, 22432–22439.

23 R. Wang, Y. Sun, A. Brady, S. Fleischmann, T. B. Eldred, W. Gao, H. W. Wang, D. en Jiang and V. Augustyn, *Adv Energy Mater*, 2021, **11**, 2003335.

24 R. E. Schaak and T. E. Mallouk, *Chemical Communications*, 2002, **2**, 706–707.

25 M. Kudo, H. Ohkawa, W. Sugimoto, N. Kumada, Z. Liu, O. Terasaki and Y. Sugahara, *Inorg Chem*, 2003, **42**, 4479–4484.

26 N. Habbache, N. Alane, S. Djerad and L. Tifouti, *Chemical Engineering Journal*, 2009, **152**, 503–508.

27 S. Xing, W. Li, B. Liu, Y. Wu and Y. Gao, *Chemical Engineering Journal*, 2020, **382**, 112837.

28 C. Peng, C. Shen, S. Zheng, W. Yang, H. Hu, J. Liu and J. Shi, *Nanomaterials*, 2017, **7**, 326.

29 S. Pu, Y. Hou, H. Chen, D. Deng, Z. Yang, S. Xue, R. Zhu, Z. Diao and W. Chu, *Catalysts*, , DOI:10.3390/catal8060251.

30 S. H. Zhang, M. F. Wu, T. T. Tang, Q. J. Xing, C. Q. Peng, F. Li, H. Liu, X. B. Luo, J. P. Zou, X. B. Min and J. M. Luo, *Chemical Engineering Journal*, 2018, **335**, 945–953.

31 V. Fernandez, N. Fairley and J. Baltrusaitis, *Appl Surf Sci*, , DOI:10.1016/j.apsusc.2020.148031.

32 R. Ludmerczki, S. Mura, C. M. Carbonaro, I. M. Mandity, M. Carraro, N. Senes, S. Garroni, G. Granozzi, L. Calvillo, S. Marras, L. Malfatti and P. Innocenzi, *Chemistry - A European Journal*, 2019, **25**, 11963–11974.

33 S. Oswald, F. Thoss, M. Zier, M. Hoffmann, T. Jaumann, M. Herklotz, K. Nikolowski, F. Scheiba, M. Kohl, L. Giebeler, D. Mikhailova and H. Ehrenberg, *Batteries*, , DOI:10.3390/batteries4030036.

34 A. v Shchukarev and D. v Korolkov, *Central European Science Journals*, 2004, **2**, 347–362.

35 S. Yokoyama, K. Tanaka, I. Toyoshima, K. Miyahara, K. Yoshida and J. Tahshiro, *Chemical Society of Japan*, 1980, 599–602.

36 D. Majhi, A. Kumar Mishra, K. Das, R. Bariki and B. G. Mishra, *Chemical Engineering Journal*, 2021, **413**, 1227506.

37 Q. Xu, R. Li, C. Wang and D. Yuan, *J Alloys Compd*, 2017, **723**, 441–447.

38 F. Xu, H. Chen, C. Xu, D. Wu, Z. Gao, Q. Zhang and K. Jiang, *J Colloid Interface Sci*, 2018, **525**, 97–106.

39 Q. Yuan, L. Chen, M. Xiong, J. He, S. L. Luo, C. T. Au and S. F. Yin, *Chemical Engineering Journal*, 2014, **255**, 394–402.

40 M. Kebir, A. Boudjemaa, Y. Azoudj, M. Sehailia and K. Bachari, *Canadian Journal of Chemical Engineering*, 2018, **96**, 2292–2298.

41 L. Shi, Z. Li, K. Marcus, G. Wang, K. Liang, W. Niu and Y. Yang, *Chemical Communications*, 2018, **54**, 3747–3750.